Nano Energy 129 (2024) 110082

Contents lists available at ScienceDirect

Nano Energy

journal homepage: www.elsevier.com/locate/nanoen

Full paper

One-step fabrication of functionalized electrodes on 3D-printed polymers for triboelectric nanogenerators

Semih Akin [a,*,1], Taehoo Chang [b,1], Sk Shamim Hasan Abir [a,1], Young Won Kim [c,d], Shujia Xu [e], Jongcheon Lim [f], Yuseop Sim [c], Jiho Lee [c], Jung-Ting Tsai [g], Chandra Nath [h], Hyowon Lee [f], Wenzhuo Wu [e], Johnson Samuel [a], Chi Hwan Lee [b,c,f,i,**], Martin Byung-Guk Jun [c,*]

[a] Department of Mechanical, Aerospace and Nuclear Engineering, Rensselaer Polytechnic Institute, Troy, NY 12180, USA
[b] School of Materials Engineering, Purdue University, West Lafayette, IN 47907, USA
[c] School of Mechanical Engineering, Purdue University, West Lafayette, IN 47907, USA
[d] Advanced Joining & Additive Manufacturing R&D Department, Korea Institute of Industrial Technology, 15014, the Republic of Korea
[e] School of Industrial Engineering, Purdue University, West Lafayette, IN 47907, USA
[f] Weldon School of Biomedical Engineering, Purdue University, West Lafayette, IN, USA
[g] Department of Mechanical Engineering, National Taiwan University of Science and Technology, Taipei 106335, Taiwan, ROC
[h] Environmental and Ecological Engineering Department, Purdue University, West Lafayette, IN 47907, USA
[i] Elmore Family School of Electrical and Computer Engineering, West Lafayette, IN 47907, USA

ARTICLE INFO

Keywords:
Triboelectric nanogenerator (TENG)
Polymer metallization
Cold spray
Additive manufacturing
Rapid prototyping
Polymer electrode
Polylactic acid

ABSTRACT

Triboelectric nanogenerators (TENGs) have gained remarkable attention in energy harvesting and smart sensing, allowing for converting mechanical energy into electrical energy. Despite great potential and progress made in this field, there remains a high demand for high-performance electrodes that are produced with sustainable, low-cost, lightweight, and durable materials such as polymers. Here, by combining the material extrusion 3D printing and the cold spray particle deposition methods, we employ a complete additive manufacturing (AM) approach to fabricate functionalized electrodes on 3D-printed parts for TENG technology. First, polylactic acid (PLA) parts were produced by material extrusion printing. Next, the cold spray process (CS) was utilized as just a one-step fabrication method of the conductive electrodes on the printed parts, eliminating the need for surface activation, over-plating, curing, and/or post-processing. Additionally, the process-structure-property relationships of the CS process were uncovered to fabricate high-performance electrodes for TENGs. The resulting electrodes demonstrate promising electrical conductivity (9.8×10^4 S.m^{-1}), adhesive strength, stability, and micro-roughness (R_a = 6.32 μm). The TENG with the fabricated electrode generates an open-circuit voltage of 174 V, which is nearly 1.85–2.9-fold higher than that of the control TENGs. It achieves the short-circuit density of ≈ 55 mA/m^2, and the power density of 1676 mW/m^2. Besides, to address the low-spatial resolution of the cold spray metallization, a manufacturing pathway is proposed, aiming to achieve higher line resolution (1 mm linewidth) electrodes for polymer electronics. This work provides a manufacturing strategy that can advance the field of TENG and polymer electronics by addressing the limitations of conventional electrode manufacturing techniques.

1. Introduction

Triboelectric nanogenerator (TENG) – a state-of-the-art energy harvesting device – presents opportunities to effectively harness abundant surrounding mechanical energy sources into electrical energy [1,2]. Owing to its high efficiency, simplicity, and low cost, TENG has been proven as a viable energy harvesting technology in many applications, including micro/nano energy harvesting [3], active and smart sensing [4,5], self-powered sensors [6], smart home applications [7], blue

* Corresponding authors.
** Correspondence to: Weldon School of Biomedical Engineering, School of Mechanical Engineering, School of Materials Engineering, Elmore Family School of Electrical and Computer Engineering, Purdue University, West Lafayette, IN 47907, USA.
E-mail addresses: akins@rpi.edu (S. Akin), lee2270@purdue.edu (C.H. Lee), mbgjun@purdue.edu (M.B.-G. Jun).
[1] S.A., T.C., and S.H.A contributed equally to this work.

https://doi.org/10.1016/j.nanoen.2024.110082
Received 24 June 2024; Received in revised form 26 July 2024; Accepted 2 August 2024
Available online 3 August 2024

Nomenclature

A	Area
L	Length
R	Resistance
R/R_0	Relative resistance
R_s	Sheet resistance
S	Siemens
ρ	Resistivity
Ω	Ohm

Abbreviations

AM	Additive manufacturing
CS	Cold spray
CSC	Charge storage capacity
CV	Cyclic voltammetry
EDX	Energy-dispersive X-ray
I_{sc}	Short-circuit current
ITO	Indium tin oxide
ITO-PET	ITO coated polyethylene terephthalate
LED	Light emitting diode
Pd	Palladium
PLA	Polylactic acid
PTFE	Polytetrafluoroethylene
RT	Room temperature
SEM	Scanning electron microscopy
Sn	Tin
V_{oc}	Open-circuit voltage

energy [1], etc. The working mechanism of TENG lies in contact electrification and electrostatic induction [8]. In principle, when two materials with opposite polarities come into contact and then separate or slide each other, electron transfer takes place between the materials, which can be harvested through an external circuit [3]. Herein, the output performance of TENG strictly relies on electrostatic induction between the friction layers and electrodes [9,10]. In this regard, many attempts have been made to improve the TENG performance by employing various materials, such as metal films, polymers, composites, and micro- and nanostructured materials [11–13].

Among others, electrodes on polymer substrates are of particular interest to improve energy harvesting efficiency for TENG as they are sustainable, durable, lightweight, and low-cost [14–16]. These electrodes are mainly produced by lithography [17], vapor deposition [18], screen printing [19], ink-jet printing [20], and laser-induced metallization [21]. In these methods, functional materials are deposited on the base polymeric substrate to constitute conductive electrodes embedded on the surface. An ideal polymer electrode for high-performance TENG should possess: i) micro-rough surface morphology to increase the contact area; ii) strong adhesive strength between the functional surface coating and substrates; iii) stable electrical conductivity; and iv) durability under severe friction. All these features are integral to creating high-performance and durable TENGs. However, traditional manufacturing methods face challenges in creating high-performance electrodes due to the need for additional sources or processes, such as high temperature, vacuum, over-plating (*e.g.*, electroless deposition), precursor, or post-sintering processes.

As shown in Fig. 1**a**, the traditional manufacturing process of functional electrodes on polymer substrates lies in the metallization process, often involving environmentally hazardous surface pretreatment and

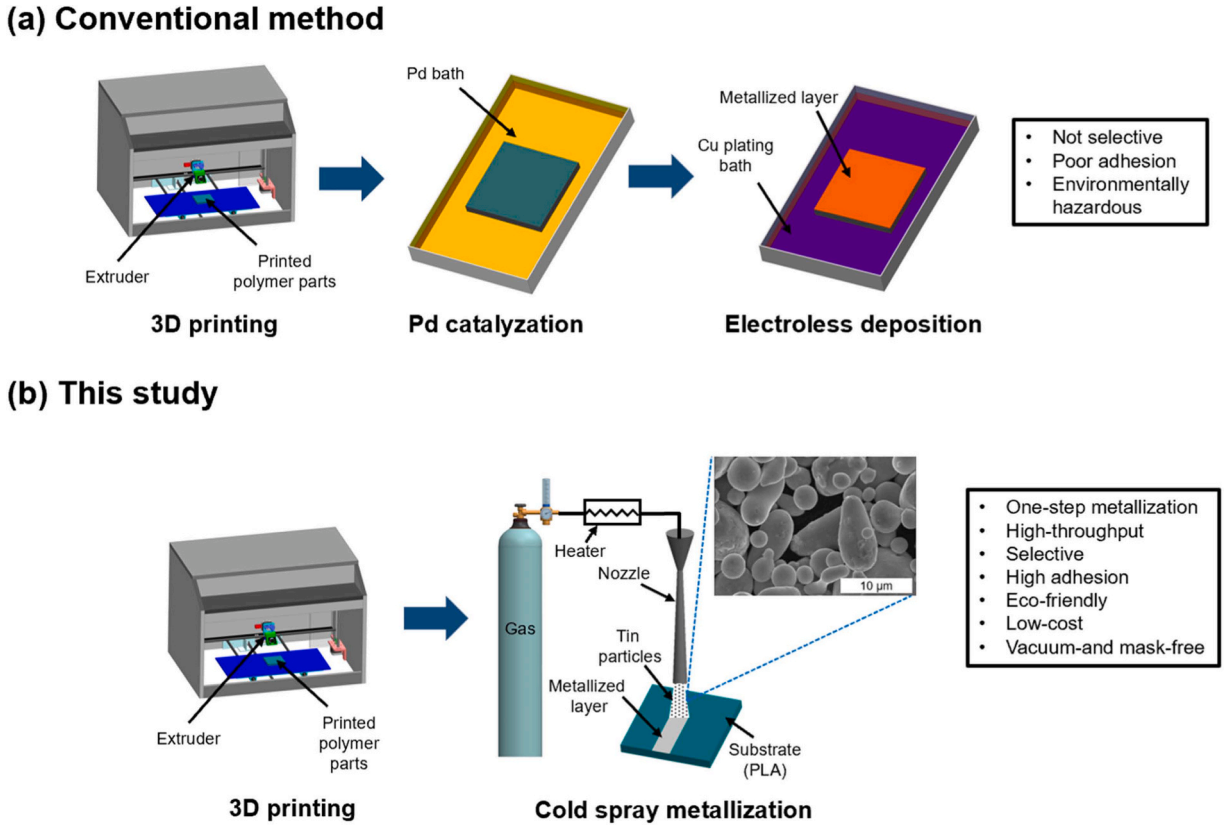

Fig. 1. Schematics of the **(a)** traditional polymer metallization approach; **(b)** the additive manufacturing approach in this study.

cost-intensive palladium (Pd) seeding processes [22]. These demanding surface treatment processes impede the sustainable utilization of this approach in producing functionalized electrodes on polymer parts. Recently, additively manufactured electrodes have gained considerable attention in energy harvesting applications [23] due to their flexible, accurate, and low-cost manufacturing practices through rapid prototyping [24–26]. Particularly, commercial conductive filaments (*e.g.*, Proto Pasta, Black Magic, Electrifi) enabled rapid prototyping of 3D-printed electrodes [27,28]. However, these conductive filaments have poor conductivity, which is generally 3750 times lower than the standard bulk copper (*i.e.*, 58.7×10^6 S.m^{-1}) [29], thereby limiting the utilization of the 3D-printed electrodes in energy harvesting applications. Some studies [30–32] integrated 3D printing with conductive filaments and subsequent surface metallization process through electroless or electro-plating. Even though these attempts led to improved electrical conductivity, these methods often employ cost-intensive catalyst (*e.g.*, palladium) embedded filaments with additional process steps such as over-plating. As such, a critical need is identified for the non-traditional additive manufacturing (AM) method that may enable sustainable and high-throughput production of functionalized electrodes embedded on 3D-printed polymers for energy harvesting applications, including TENGs and the like.

Recently, the authors' group has deployed and studied the emerging cold spray (CS) particle deposition technique to create enhanced-performance TENGs [6,33]. In these studies, functional surfaces were produced on flexible polymers (*i.e.*, PTFE, PET films) as the triboelectric friction layer and electrode. Furthermore, the CS process has been recently proposed to create counter electrodes on 3D-printed polymers for dye-synthesized solar cell applications [34]. These initial proof-of-the-concept results revealed the remarkable potential of the CS in the field of energy harvesting. Building on these earlier findings, this study, as shown in Fig. 1**b**, employs the CS technique to achieve one-step fabrication of functionalized electrodes on 3D-printed polymers. Furthermore, the study investigates the process-structure-property relationships of CS for TENGs and polymer electronics.

Initially, the polymer substrate is rapidly prototyped through material extrusion. Subsequently, fine metal particles are directly written on the as-printed polymer surface via the CS to create the functionalized electrodes (Fig. 1**b**). Owing to the unique properties of the CS- including low-process temperature, high-adhesion strength, corrosion resistance, and durability [35–37]- this approach ensures the creation of sustainable and high-performance electrodes on 3D-printed polymer parts. The resulting electrodes are characterized in terms of microstructure, electrical conductivity, adhesion strength, stability, and catalytic activity. Furthermore, TENG devices are fabricated to evaluate the performance of the electrodes against traditional electrode material such as aluminum. Lastly, a manufacturing pathway is proposed to address the low-spatial resolution of the CS metallization, aiming to achieve higher line resolution electrodes (1 mm linewidth). The proposed manufacturing approach further underscores the potential of the CS technique in polymer electronics. As such, this study unveils the potential of a complete AM approach that allows for one-step functional metallization of 3D-printed polymers in the realm of polymer electronics and energy harvesting with TENGs.

2. Experimental section

2.1. Materials

Polylactic acid (PLA) filament was used for rapid prototyping of the polymer substrate through the material extrusion 3D printing method. PLA was chosen as the substrate due to its recyclability, composability, and low melting point, all of which make PLA a highly desired material in numerous applications [38]. Moreover, PLA is favorably positioned in the triboelectric series, tending to acquire positive charge when rubbed against counter materials [39]. Additionally, PLA can function as both negative and positive material in TENG applications, depending on its counter material [40]. Notably, PLA's biodegradability and ease of printing make it particularly attractive for triboelectric energy harvesting applications. It was also demonstrated that conductive carbon filled PLA can be used to create fully enclosed microbead-structured TENG arrays, resulting in enhanced energy harvesting performance [41].

In the CS process, tin (Sn) powders were selected as the feedstock material due to its low strain hardening and high softening rates [42,43]. These properties facilitate metallurgical bonding of Sn particles onto the polymer surface compared to the pure aluminum (Al) powders. As such, achieving electrically conductive layers (electrodes) on 3D-printed parts using Al particles poses challenges in contrast to Sn feedstock, resulting in inferior performance in TENG applications (see Fig. S1, Supporting Information). Additionally, Sn has high corrosion resistance, making it as a promising functional material for TENGs and polymer electronics [6,44]. Taken together, Sn powders were chosen in this study to fabricate CS-based electrodes in TENG applications. The morphology of the Sn powders is shown in Fig. 1**b** (right panel), having a quasi-spherical shape in a size range of 10–45 μm [43]. In TENG fabrication, PLA substrate with a thickness of 1 mm was cold sprayed to deposit Sn electrode. Conventional Al foil with two different thickness, ≈152 μm (*McMaster, Part No: 9708K56*) and 16 μm (*Reynolds*), was employed in the control TENGs as the electrode material for performance studies. Notably, 152 μm-thick Al film has a comparable thickness to the as-CS Sn electrode, while the 16 μm-thick Al film was used for further characterization, as it is falls within the widely-used thickness range for friction layers in TENG applications. All the materials used, including those for the cyclic voltammetry test and TENG fabrication for performance comparison, are 'as-received' without any further purification as listed Table 1.

2.2. Methodology

Fig. 1**b** illustrates the proposed AM approach of functionalized electrodes deposited on the 3D-printed polymer parts. First, the polymer substrate (PLA) is rapidly prototyped through material extrusion. Next, the polymer surface is directly metallized by the CS method. Unlike the traditional polymer metallization methods, the proposed approach enables one-step metallization of 3D-printed parts without the need for environmentally hazardous strong acid etching and cost-intensive Pd absorption processes. Moreover, owing to the unique properties of the CS, including low-process temperature, high-adhesion strength, and minimal thermal degradation, this approach ensures sustainable and high-throughput surface metallization on 3D-printed parts in a selective, cost-effective, and vacuum-free manner. In the next sub-sections, each step in the proposed AM approach is described in detail.

2.2.1. Material extrusion 3D printing

The polymer substrates were fabricated using a rapid prototyping approach based on material extrusion due to its ease of use, prototyping accuracy, and low cost [45]. The parts are produced by a 3D printer

Table 1
Materials used in this study.

Process	Materials	Supplier
Material extrusion 3-D printing	PLA	Sindoh Inc.
Cold spray metallization	Tin (Sn) particles	Centerline Ltd.
Cyclic voltammetry (CV) test	Lithium iodide (LiO); Iodine (I_2); Lithium perchlorate ($LiClO_4$); Acetonitrile	Sigma-Aldrich
TENG fabrication (for performance comparison)	PTFE film, Polyimide, Aluminum tape, Foam tape; Reynolds aluminum foil	McMaster Amazon

(*Sindoh 3DWOX*) with a single nozzle configuration on a heated bed with a temperature of 90 ℃. The extruder temperature and the thickness of each layer were set to 200℃ and 0.2 mm, respectively. Under these 3-D printing conditions, the PLA substrate with a thickness of 1 mm was produced to be used as the electrode material in TENGs. The surface roughness of the fabricated bare PLA substrates is measured as R_a= *2.85* ± *0.75 μm*. The operational settings of the 3D printing process are presented in Table 2.

2.2.2. Cold spray (CS) direct writing

The surface of the 3D-printed PLA parts was functionally metallized for TENG application via the CS method. In this regard, micron-scale Sn particles were deposited on the PLA surface using a low-pressure CS machine (*Rus Sonic Technology, Model K205/407 R*) mounted on a programmable multi-axis robot arm to precisely control the surface deposition process. A rectangular-shaped nozzle was used in particle deposition experiments for large-area metallization owing to its larger exit aperture (10.35 mm × 3 mm). A representative image of the entire CS setting is presented in Fig. 2**a**. To investigate the process-structure-property relationships of the CS deposition on 3D-printed PLA surface, various gas conditions (*i.e.*, inlet pressure, temperature) and kinematical settings (*i.e.*, nozzle speed, spray distance) were considered as listed in Table 3.

2.3. Characterization methods

Scanning electron microscopy (*SEM, Hitachi S-4800*) was used to analyze the microstructural morphology of the resultant metallization. The chemical composition of the resultant electrodes was characterized by the energy-dispersive X-ray (EDX) (*Hitachi S-4800*). The electrical resistance of the fabricated electrodes was measured by the two-point probe method using a digital multimeter (*Agilent/HP 34401A*). Moreover, a four-point probe system (*Jandel, RM3-AR*) was used to characterize the sheet resistance. The cyclic voltammetry (CV) tests were also performed to analyze the catalytic and electrochemical activity of the electrodes through a potentiostat (*SP-200, Bio-Logic Inc, Seyssinet-Pariset, France*). The Scotch (*3 M magic tape*) tape test method was applied to investigate the adhesive strength of the electrodes. The surface roughness was measured by a surface roughness tester (*AMTAST*). A custom-build programmable pneumatic actuator, coupled with an oscilloscope (*Agilent, DSO1014A),* was used to measure the open-circuit voltage (V_{oc}). The short-circuit current (I_{sc}) was measured using a current amplifier (*Edmund Optics*) connected to the oscilloscope.

3. Results and discussion

3.1. Optimal operational conditions of the CS

Identifying optimal operational conditions for the CS is vital for precisely fabricating the electrodes on the 3D-printed parts. To achieve this, we selected and studied the governing operational parameters of the CS process in terms of driving gas pressure (P), gas temperature (T), spray distance (SD), and nozzle speed (NS). Fig. 3**a–c** present the effect of these CS parameters on the electrical resistance of the fabricated electrodes in a range of P = 0.6–0.7 MPa, T = 25–150 ℃, SD = 5 – 40 mm, and NS =100–300 mm/s. These tests were conducted for two different pressure levels at P= 0.6 and 0.7 MPa. The gas temperatures were measured near the nozzle surface close to the exit section under steady-state conditions using an infrared thermal camera (FLIR A300). The temperature distribution along the nozzle at various temperature settings is provided in Fig. S2, (Supporting Information).

Table 2
Process parameters of the material extrusion 3-D printing.

Process parameters	Value
Filament diameter (mm)	1.75
Bed temperature (℃)	60
Extruder temperature (℃)	200
Infill density (%)	80
Layer height (mm)	0.2
Print speed (mm.s^{-1})	40
First layer speed (mm.s^{-1})	10

Fig. 3**a** shows that no electrical conductivity was achieved at room temperature (25 ℃) without preheating the gas. Even though particles were locally impinged into the target surface, no continuous metallurgical bonding was observed (see Fig. S3, Supporting Information). The reasons are: i) insufficient particle impact velocity for metallurgical consolidation; and ii) poor thermal softening due to a low process temperature [46]. Conductive metallization on the polymer surface was achieved at T ≥ 80 ℃. This can be attributed to the increase in kinetic energy of particles at elevated gas temperature, which facilitated material consolidation on the polymer surface (see Fig. 4**a-b**). The colored cross-section SEM image in Fig. 4**g** also indicates that the particles effectively impinged into the polymer interface at T= 80 ℃ and P=0.7 MPa. As the gas temperature was further increased, no remarkable change in electrical resistance was observed. However, local erosions were inspected on the polymer surface due to the elevated process temperatures, such as at T = 150℃ (see Fig. S4, Supporting Information).

Regarding nozzle speed, Fig. 3**b** demonstrates that resistance tends to increase with higher nozzle speeds. It is attributed to reduced particle deposition on the polymer surface due to the short spraying time at higher nozzle speeds. The lowest resistance was achieved at the NS ≤ 150 mm/s, while resistance sharply increased at NS > 150 mm/s. The microstructure analysis in Fig. 4**c** reveals significant porosity on the target surface at NS = 250 mm/s and P = 0.6 MPa, where Sn particles are locally impinged into the polymer (see Fig. S5a, Supporting Information). The high porosity impedes the continuous junctions among the Sn particles, resulting in limited or no conductivity. Even though higher pressures (P = 0.7 MPa) at NS = 250 mm/s led to a coated surface with less porosity as shown in Fig. 4**d**, the electrical resistance significantly raised to over 100 Ω under these process conditions (see Fig. 3**b**). The cross-section SEM analyses in Fig. 4**h-i** reveal that the particles could not fully impinge into the polymer interface at NS=250 mm/s. Considering the electrical conductivity is directly related to the film thickness, this explains the poor electrical conductivity at NS > 200 mm/s. Consequently, no electrical conductivity was achieved at NS > 250 mm/s.

Fig. 3**c** presents the effect of the SD on electrical resistance at two different pressure levels. Regardless of gas pressure, the resistance tends to increase with larger spray distances (SD >10 mm). This increase is attributed to the opposing drag force at higher spray distances resulting in a significant decrease in the particles' impact velocity [47], resulting in a sparse surface deposition (Fig. 4**e**). This effect can be compensated by increasing the gas pressure, potentially leading to enhanced material consolidation on the polymer surface, as shown in Fig. 4**f**. The film thickness decreased with the increase of the SD, leading to higher electrical resistance at greater SD. Cross-section SEM analysis in Fig. S5b (Supporting Information) confirmed the poor particle impingement into the polymer interface at SD = 30 mm. Further increase in the SD beyond 30 mm resulted in disruptive particle deposition with no stable electrical conductivity (Fig. 3**c**). Notably, we observed lower electrical resistance at SD = 10 mm as compared to SD = 5 mm, suggesting that there is an optimal focal point to achieve more compact surface deposition. A SD shorter than a certain threshold often generates strong shock waves (*i.e.*, bow-shock) upon the impact of the supersonic gas jet, leading to nonuniform surface deposition [48,49]. Based on these findings along with the high-electrical conductivity and uniform metallization, the optimal CS settings were identified at P = 0.7 MPa, T = 80 ℃, NS = 100 mm/s, and SD =10 mm. The EDX analyses confirmed the effective and uniform distribution of the Sn particles over the polymer surface at the optimal CS settings (see Fig. S6, Supporting Information).

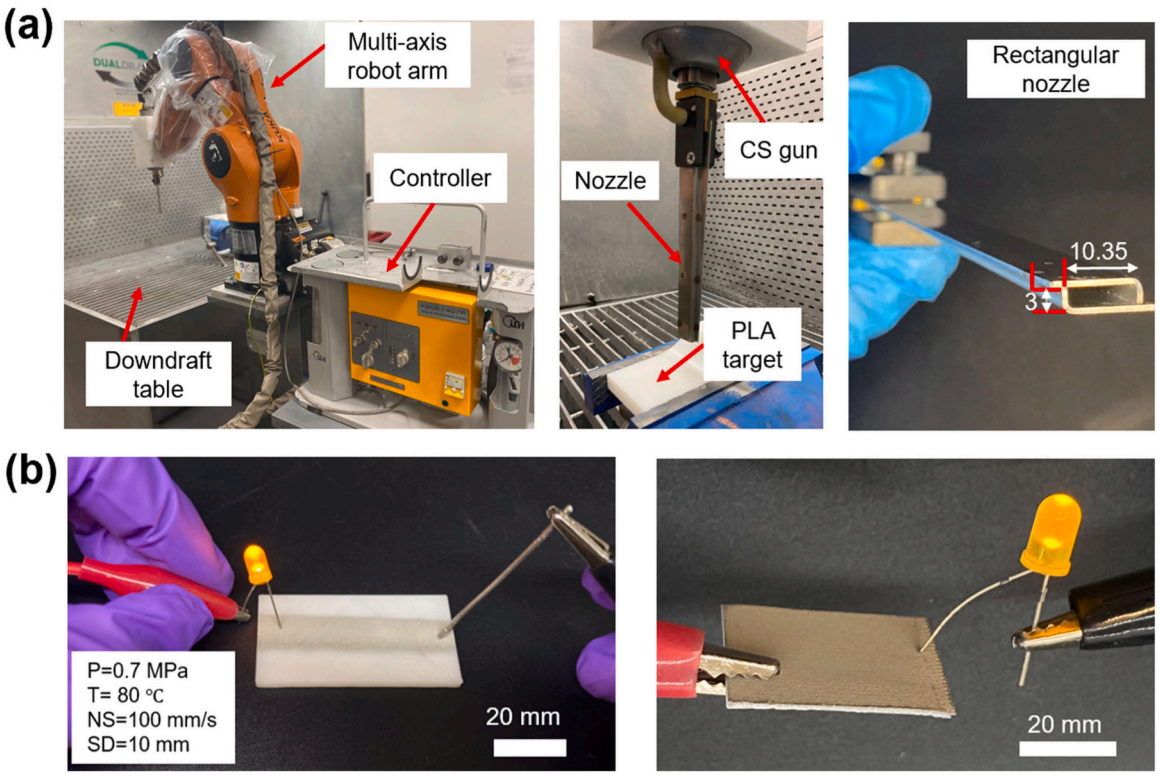

Fig. 2. Representative images of the **(a)** CS setup; **(b)** conductively metallized 3D-printed PLA parts.

Table 3
Process settings of the cold spray.

Process parameters	Value
Working gas	Air
Gas inlet pressure (MPa)	0.6, 0.7
Gas temperature (°C)	RT, 80, 120, 150
Nozzle transverse speed (mm.s^{-1})	100, 150, 200, 250, 300
Spray distance (mm)	5, 10, 20, 30, 40
Number of spray pass	1
Powder feed rate (g.s^{-1})	0.2

3.2. Electrical performance

The electrical conductivity of the electrodes was calculated by using Eq.1, where ρ is the conductivity, R is the resistance, and A is the cross-sectional area of the electrode. The length, width, and average thickness of the electrodes are 25×10^{-3} m, 20×10^{-3} m, and 142 μm, respectively. The average electrical resistance (R) of the electrode test units was measured as 0.09 Ω (see Fig. 3**a**). Collectively, the electrical conductivity of 9.8×10^{4} S.m^{-1} was achieved for the Sn electrodes, which is only two orders of magnitude lower than the bulk conductivity of Sn (*i.e.*, 9.17×10^{6} S.m^{-1}). This promising conductivity can be attributed to material consolidation and minimal porosity under the optimal CS processing conditions.

$$\sigma = \frac{L}{RA} \tag{1}$$

We also investigated the relationship between the adhesive strength and electrical stability of the fabricated electrodes by using the Scotch tape test method [21,50]. Fig. 3**d** shows the corresponding resistance of the electrodes under various Scotch tape (3 M magic tape) peeling cycles for the test units (*i.e.*, conduction path in a size of 25 mm × 20 mm). No significant change in the relative resistance (R/R_0) was observed for the electrodes. The overall increase in R/R_0 did not exceed 10 % during the peeling cycles, indicating both strong adhesive strength and electrical stability. Further qualitative characterizations, including rigorous bending deformations, confirmed the strong interfacial adhesive strength between the fabricated electrodes and the substrate (see Video S1, Supporting Information). No structural delamination or compromise in electrical conductivity was observed in the fabricated electrodes under the harsh mechanical stimuli (Video S1).

The sheet resistance (R_s) was also calculated to compare the electrical conductivity of the 3D-printed electrodes with the conventional electrodes such as FTO glass and ITO/PET (see Table 4). The R_s measurements indicate that the electrical performance of the polymer electrode is promising compared to the traditional electrodes commonly used in energy harvesting applications. Moreover, the CS-based electrode (*i.e.*, PLA/Sn) exhibits a larger surface roughness than other electrodes, which is a desirable feature in the field of TENG, as it enhances the active surface area, charge flow and charge trapping performance [2,51].

Besides, cyclic voltammetry (CV) tests were conducted to investigate the catalytic and electrochemical activity of the electrodes. In the CV tests, a three-electrode configuration was employed, consisting of: (i) Ag/AgCl with 3 M KCl as the reference electrode; (ii) Pt counter electrode, and (iii) different types of working electrodes (PLA/Sn, Al foil, ITO/PET, and FTO/glass) for performance comparison. The electrolyte (*i.e.*, acetonitrile solution with 10 mM LiI, 1 mM I_2, and 0.1 M $LiClO_4$) was prepared based on the past study [52], where the scan rate of the CV tests is 50 mV.s^{-1}. A representative image of the CV test setup is provided in Fig. S7 (Supporting Information).

Fig. 5 compares the CS electrode (PLA/Sn) over the traditional counterpart electrodes, including Al foil, FTO glass, and ITO/PET. As observed in the CV plot in Fig. 5**a**, the Sn electrode exhibited a considerably higher magnitude of reduction/oxidation curve compared to other electrodes, indicating a significantly enhanced catalytic activity. To further compare electrochemical performance at the electrode/electrolyte interface, the charge storage capacity (CSC) was calculated based on the past study [53]. The CSC quantifies and assesses the amount of charge that can be stored within the electrode material. As

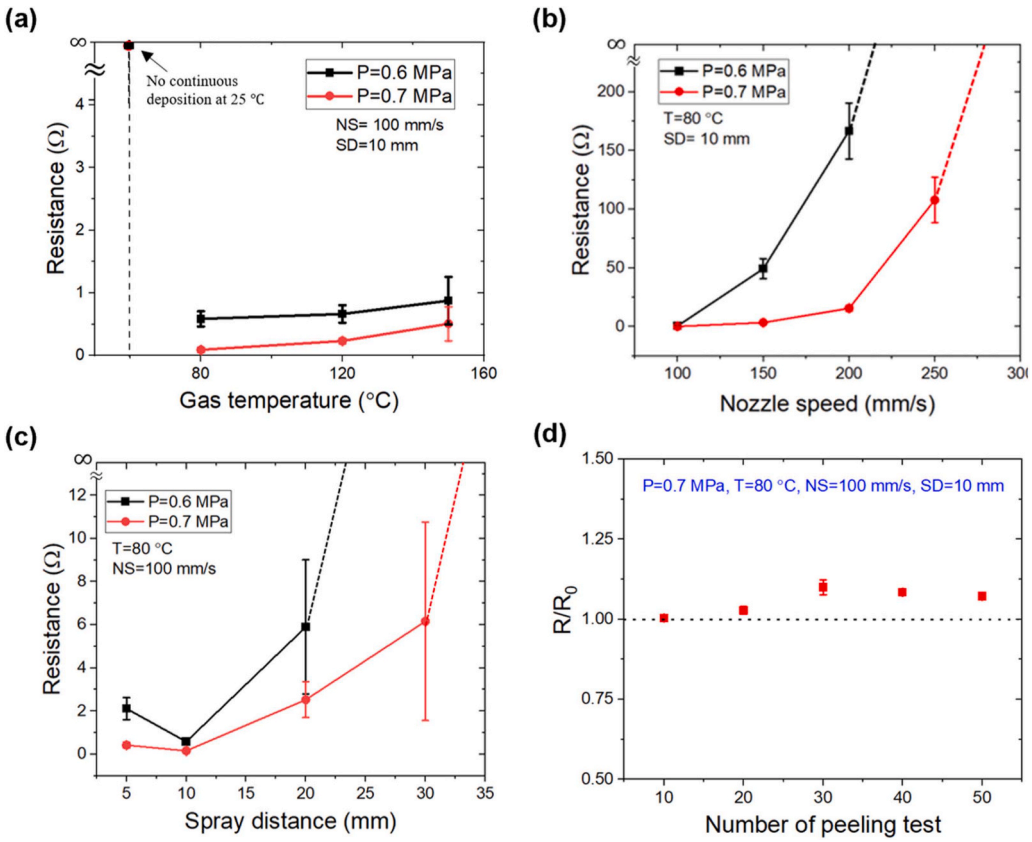

Fig. 3. **(a)** Effect of the gas temperature and gas pressure; **(b)** Effect of the nozzle speed; **(c)** Effect of the spray distance on the electrical resistance of the resultant coating; **(d)** Relative resistance (R/R_0) change of the electrodes under peeling tests; (The electrode length (L) = 25 mm and width (w) = 20 mm).

shown in Fig. 5**b**, the CSC of the Sn electrode (9.0 ± 1.4 $mC.cm^{-2}$) is significantly higher (up to 570 times as in Al) compared to the counterpart electrodes. This enhancement can reasonably be attributed to the enlarged electrochemical active surface area resulting from the micro-rough surface morphology of the PLA/Sn electrode. This phenomenon significantly enhanced the electrode's capability for charge interaction within an electrochemical cell, leading to a promising CSC for the PLA/Sn electrode.

3.3. Fabrication of the TENGs

The contact-separation mode TENG design was considered owing to its simple structure with facile fabrication as well as widespread acceptance in TENG literature [54]. As shown in Fig. 6**a**, the complete working cycle of a contact-separation mode TENG consists of four main steps. In the initial state, where there is no contact, charge transfer does not occur between the materials. When an input pressure is applied, the positive and negative layers come into contact, leading to charge polarization at the materials' surface. Upon releasing the load, the material starts separating from each other. This separation creates a potential difference between the positive and negative friction layers, driving electrons from the friction layers to the charge collectors (electrodes) through an external circuit. This process enables the cyclic conversion of applied external mechanical energy into electrical energy by the TENG.

In a vertical-contact separation mode TENG, the output voltage (V) can be determined using Eq.2 [55], where Q is the transferred charge, S is the contact surface area, σ is the triboelectric surface charge density, d is the thickness of the layers, ε is the relative dielectric constants of the triboelectric layers, ε_0 is the vacuum permittivity, and x is the distance between the layers (*i.e.*, separation distance).

$$V = -\frac{Q}{S\varepsilon_0}\left[\frac{d_1}{\varepsilon_{r1}} + \frac{d_2}{\varepsilon_{r2}} + x(t)\right] + \frac{\sigma x(t)}{\varepsilon_0} \tag{2}$$

Under the open-circuit conditions, where no charge transfer occurs (*i.e.*, Q=0), the open-circuit voltage (V_{oc}) can be calculated from Eq.3 as expressed below [55]. This V_{oc} depends on the triboelectric charge density, distance between the triboelectric layers, and the vacuum permittivity.

$$V_{oc} = \frac{\sigma x(t)}{\varepsilon_0} \tag{3}$$

In our study, we designed and fabricated contact-separation mode TENGs using various material configurations for performance evaluation tests. A representative image of the fabricated TENG is shown in Fig. 6**b**, with PLA serving as the negative layer and CS/Sn acting as the back-electrode on the PLA surface. Additionally, the traditional Al electrode was employed in TENG devices as the control group for performance comparison. Fig. 6**c** presents the fabricated TENGs with various material configurations and their respective thickness for performance testing. 152 μm-thick Al film was employed in control TENGs (i.e., Design I and Design III) as it has a comparable thickness to the CS/Sn electrode (Fig. 4**g**). Both Design I and II utilize the Al film as the positive friction layer and electrode while the PLA polymer is the negative layer. The main distinction between Design I and II lies in the back-electrode of the negative triboelectric material (PLA). Specifically, Design I employs the Al film as the back-electrode while Design II incorporates the CS/Sn electrode. Subsequently, we compared the energy harvesting performance of TENGs with Design I and Design II, evaluating the CS/Sn electrode against the traditional Al electrode.

Furthermore, the PLA/Sn electrode was also tested as the back-electrode of the tribo-positive material. Considering the triboelectric series [56], PLA can favorably function as the tribo-positive material as

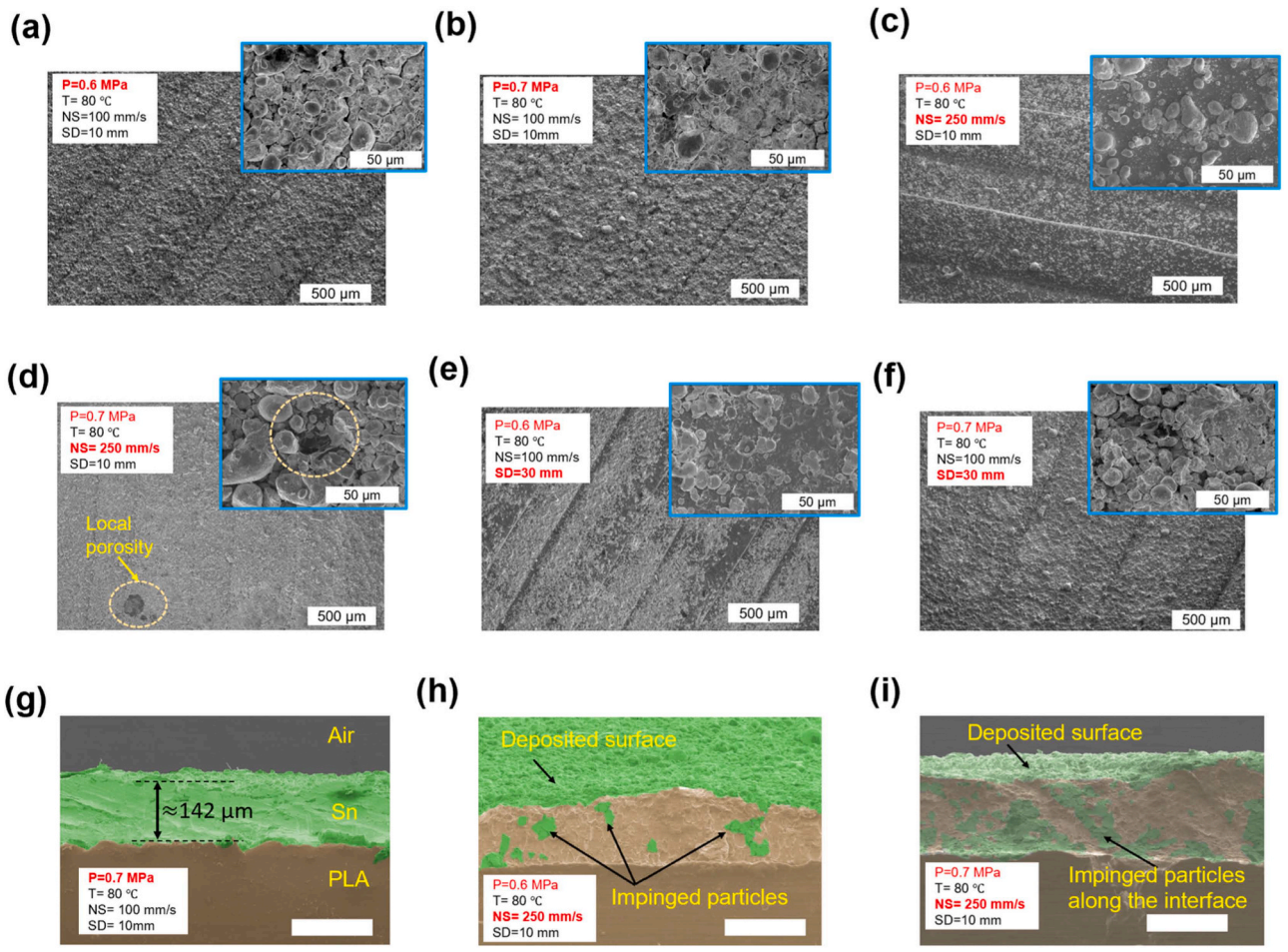

Fig. 4. Characterization of surface microstructure at various CS settings. **(a–f)** Surface microstructure; **(g–i)** Cross-section microstructure (The CS settings are provided in each figure within an enclosed white box).

Table 4
Electrical performance and surface roughness **c**omparison of the fabricated electrode with other electrodes.

Electrode material	Two-point resistance (R), (Ω)	Average sheet resistance, R_s (Ω/sq)	Average surface roughness (R_a), µm
CS Sn/PLA*	0.11 ± 0.005	0.029 ± 0.008	6.316 ± 0.867
FTO/glass	37 ± 0.535	7 [66]	0.1718 ± 0.071
ITO/PET	233.7 ± 40	60 [67]	0.178 ± 0.032
Al film	0.09 ± 0.004	0.0034 [68]	0.3965 ± 0.112

it tends to lose electrons when in contact with another material, becoming positively charged. The triboelectric properties of materials like PLA have practical applications in the field of triboelectric energy harvesting, where the contact and separation of materials are harnessed to generate electricity [57]. For these experiments, as shown in Design III and IV (see Fig. 6**c**), the PTFE (Teflon) film was utilized as the negative layer due to its broad applicability in achieving stable and high-performance triboelectric energy harvesting [58]. The primary distinction between Design III and IV lies in their positive back-electrode, with Design III featuring an Al back-electrode, while Design IV incorporates the CS/Sn as the back-electrode for performance comparison. For all devices, polyimide (Kapton film, thickness = 1.25 mm) was used as the substrate material due to its inherent elasticity for the load cycles. The friction layers were prepared in dimensions of 25.4 mm × 25.4 mm, resulting in a triboelectric contact area is 645 mm^2. The distance (gap) between the tribo-negative and tribo-positive materials was kept constant at 25 mm. In all TENGs, the PLA substrate has a thickness of 1 mm.

3.4. Performance evaluation of the TENGs

The performance of the TENGs was tested by using a custom-build programmable pneumatic actuator coupled with an oscilloscope (see Fig. S8, Supporting Information). The surface area of the piston impacting the TENGs is 0.0058 cm^2 (i.e., 76.2 mm × 76.2 mm). The pneumatic air pressure was maintained at 30 psi (≈0.2 MPa) with an actuator frequency of 1 Hz (see Video S2). Fig. 7**a** depicts the open circuit voltage (V_{oc}) generation of the TENGs. Initially, we conducted tests to compare the performance of the TENGs with Al foil as the positive layer and electrode (Design I-II). The TENG with the CS/Sn electrode (Design II) exhibited significantly better performance (i.e., peak-to-peak voltage generation) than the control TENG having the conventional Al back-electrode (Design I). The voltage generation was increased by 2.9-fold (i.e., from 32.76 V to 95 V) when employing the CS/Sn electrode as the negative back-electrode (see black and red lines in Fig. 7**a**). Furthermore, we also tested the Sn electrode as the back-electrode of the tribo-positive material (Design IV) against the TENG with Al back-electrode on the positive tribo-material of PLA (Design III). As shown in Fig. 7**a** (represented by blue and green lines), the peak-to-peak voltage generation improved by nearly 1.85-fold (*i.e.*, from ≈94 to ≈174 V) compared to the control TENG (*i.e.*, blue curve in Fig. 7**a**).

The TENG configurations in Fig. 6**c** were further characterized by employing a thinner Al foil (16 µm-thick) as the back electrode against the as-CS Sn electrodes, as it falls within the widely used thickness range

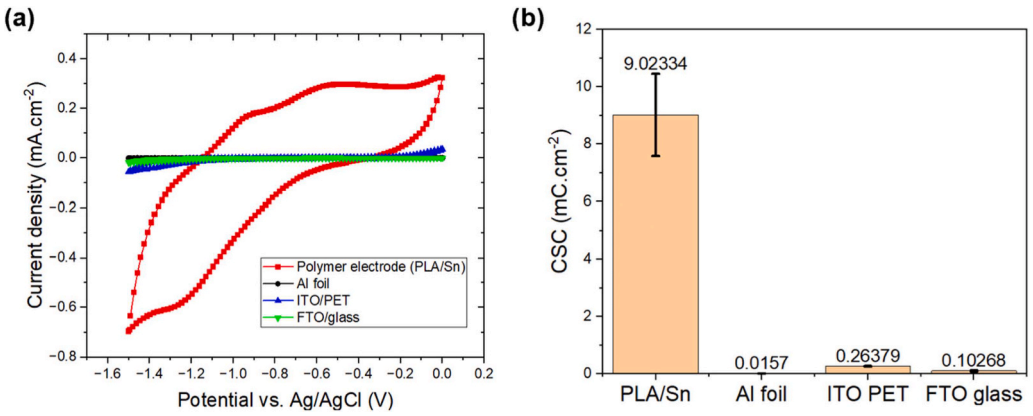

Fig. 5. **(a)** Cyclic voltammetry (CV) curves; **(b)** corresponding CSC values of the electrodes.

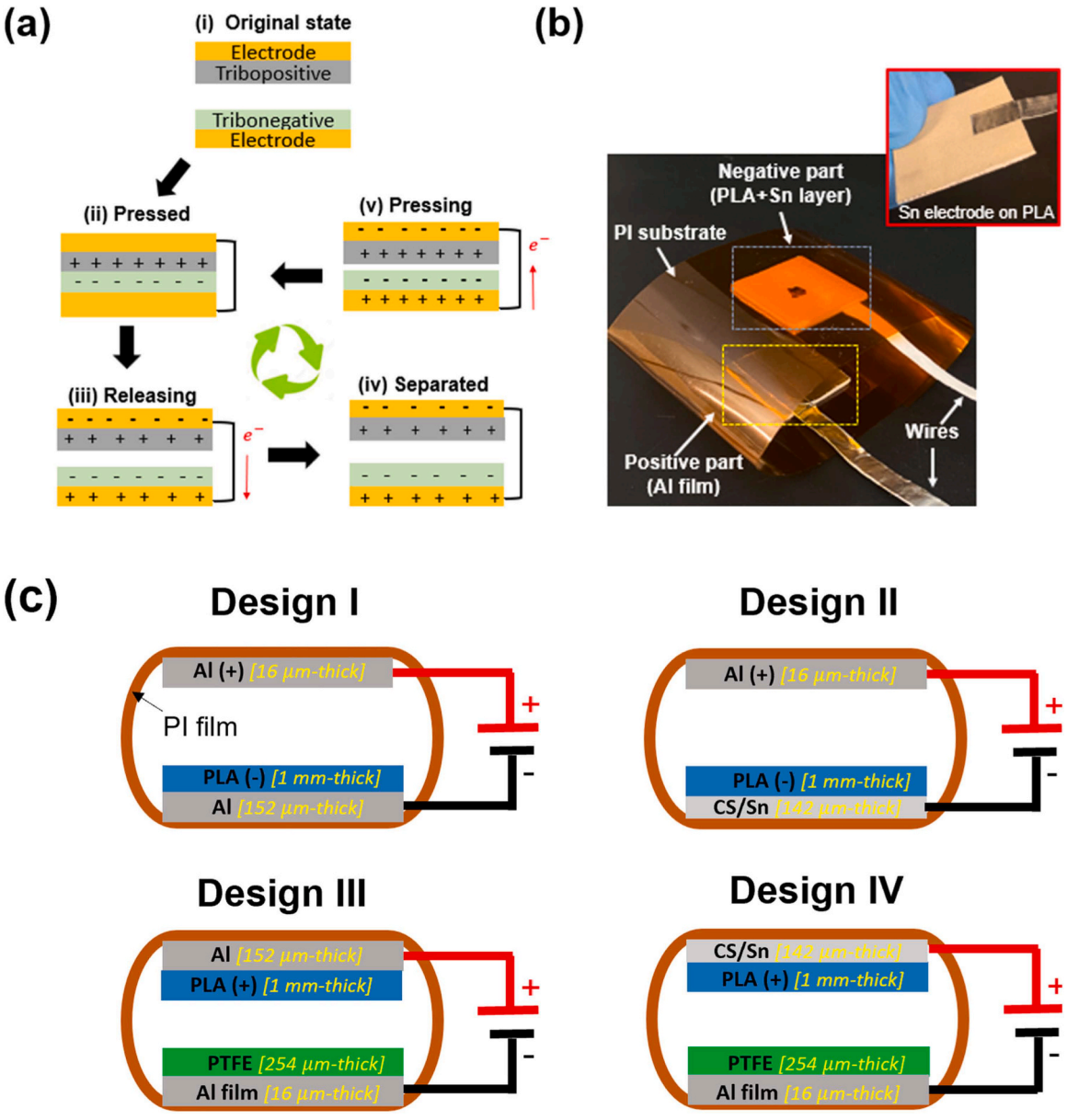

Fig. 6. **(a)** Schematic of the energy harvesting process in a full cycle of contact-separation mode TENG; **(b)** Representative image of the fabricated TENG with the PLA/Sn electrode; **(c)** Schematic of the TENGs with various material configurations.

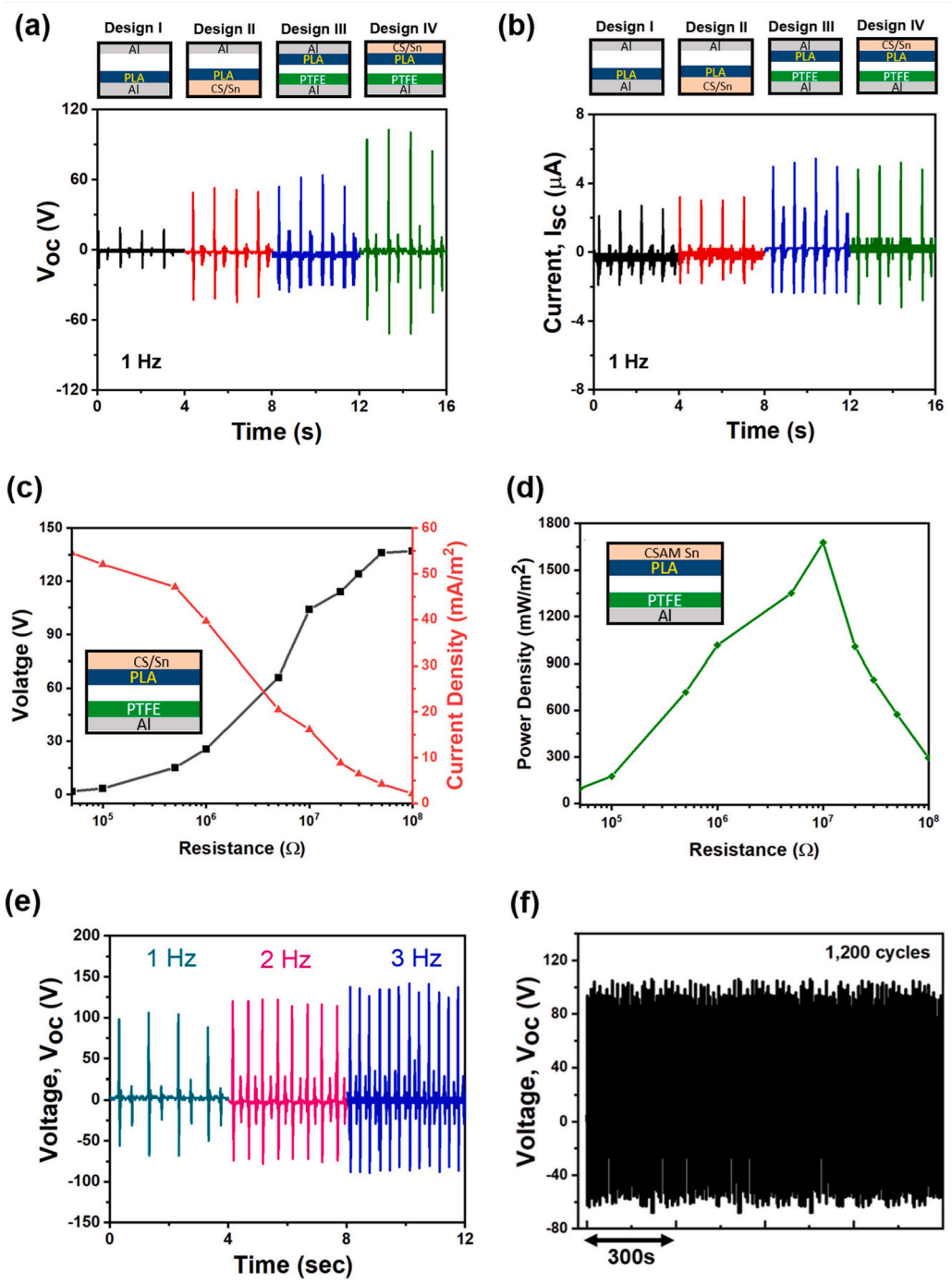

Fig. 7. **(a)** Open-circuit voltage; and **(b)** Output current; **(c)** Triboelectric output voltage and current density; **(d)** Power density; **(e)** frequency dependency; and **(f)** durability of the TENGs.

for back electrodes. The CS/Sn electrodes outperformed the 16 μm-thick Al film, demonstrating 2.8-fold higher voltage generation performance. Further details regarding this characterization study are provided in the Supporting Information (Fig. S9). Consequently, the as-CS Sn electrodes outperformed the Al electrodes in TENGs with various material and thickness configurations.

The reasons behind this enhanced performance of the TENGs with the CS electrodes can be attributed to three factors: (i) improved charge flow at the interface between the PLA layer and Sn electrode due to the strong adhesive strength; (ii) the micro-rough surface morphology of the Sn electrode; and (iii) the positive charge density of the Sn electrode embedded within the 3D-printed PLA parts. The short-circuit current (I_{sc}) measurement results in Fig. 7**b** also confirmed the improved current flow of the TENGs with the CS/Sn electrode. As for the surface roughness, the Sn electrode possesses significantly higher roughness (R_a=6.32 μm) compared to the conventional Al electrode (R_a=0.23 μm) (see Table 4). Increased surface roughness enhances the capacitance, dielectric constant, and dipole moment of the friction layers during the contact, leading to additional triboelectric charges [59]. The adhesion strength between the back-electrode and triboelectric layer is another critical factor influencing the TENG's output performance, as an optimal contact area is essential for maximizing charge accumulation and transfer [60]. Taken together, all these phenomena led to improved triboelectric synergy and charge trapping for the CS/Sn electrode.

We also investigated the effect of Sn electrode thickness on the TENG performance. The comparison of V_{oc} generation of the TENGs with varying electrode thickness is provided in Fig. S10 (Supporting Information). A quasi-linear relationship was observed between the film thickness and voltage generation, with increased film thickness leading to improved voltage generation in the TENG (Design IV) (Fig. S10c). This improvement is likely attributed to enhanced: (i) electrical conductivity due to the larger cross-section area; (ii) charge storage capacity due to its larger volume and increased capacitance. According to the resistivity formula (i.e., $R = \rho L/A$), the increased cross-sectional area decreases the electrical resistance. Consequently, the thicker Sn electrode allowed charge to flow more easily from the positive tribolayer to the back electrode, resulting in improved voltage generation performance.

Triboelectric voltage output and power generation were also characterized for the TENGs (Design IV), which features the Sn electrode as the back-electrode of the tribo-positive side. The TENG was connected to a rectification bridge and a series of resistors (see Fig. S11, Supporting Information) to obtain DC voltage, current density, and power density curves at various load resistance, ranging from 50 kΩ to 100 MΩ. Fig. 7**c-d** depict the voltage and power density of the TENG at various external load resistances. As expected from Ohm's law (V=IR), the output voltage increased with increasing resistance, while the current decreased. The maximum voltage was obtained as 137 V at the load resistance of 100 MΩ. Regarding current density measurements, the TENG exhibited a maximum current density of ≈ 55 mA/m^2 at the load resistance of 50 kΩ (Fig. 7**c**). The maximum power density of ≈ 1676 mW/m^2 was achieved at a resistance of 10 MΩ (Fig. 7**d**).

To further study the performance of the TENG, the effect of excitation frequency on the open-circuit voltage was tested under the various working frequencies, as shown in Fig. 7**e**. As the frequency increased from 1 to 3 Hz, the peak output voltage consistently rose (i.e., 174 V at 1 Hz, 200 V at 2 Hz, 227 V at 3 Hz). This increase can be attributed to increased contact per unit time at higher frequencies, which in turn improved the charge transport between the friction layers and electrodes [61]. The stability and durability of the TENG were also tested at 1 Hz loading frequency, as shown in Fig. 7**f**. No significant deterioration in the TENG's performance was observed over a working duration of 1200 s (1200 cycles), confirming the robustness and mechanical durability of the TENG.

A TENG-driven LED circuit was also designed and tested to demonstrate the pragmatic application of the fabricated electrodes (Fig. S12, Supporting Information). The TENG was connected to a rectification bridge to convert the AC output into DC voltage (Fig. S12a**)**. A 100nF capacitor was connected in parallel to the output load to be charged while TENG was hand tapped. By exerting a hand tapping force on the TENG around 15–20 times each time, 28 Light Emitting Diodes (LEDs) (each 2.0 volts) were effectively illuminated (Video S3 and Fig. S12b, Supporting Information).

Taken together, the results underscore the potential of the fabricated electrodes in enhancing the electricity harvesting performance of TENG. Notably, owing to its intrinsic electrical and mechanical properties with sustainable and facile manufacturing practices, electrodes fabricated on 3D-printed parts have the potential to serve as high-performance charge collectors in a broad array of cutting-edge energy harvesting and storage devices, including solar cells, lithium-ion batteries, supercapacitors, and more. Additionally, the established manufacturing platform could be adapted to produce polymer electronics for emerging fields such as surface-mounted devices and the Internet of Things (IoT), provided that the line resolution of the CS technique is enhanced.

While CS offers unique advantages such as high-throughput, low process temperature, adhesion strength, and corrosion resistance, it faces a challenge in spatial resolution compared to other printing techniques like inkjet and aerosol printing. This limitation stems from the nozzle dimensions of the CS equipment, which typically are around ϕ mm for round nozzles and 10 mm × 3 mm for rectangular nozzles [62, 63]. Although micro-cold spray technologies have been developed for high-resolution patterning, they require a dedicated vacuum environment to deposit functional materials on the target surface [64]. Besides, shadowing masks were also proposed to improve the line resolution of the CS process on polymer targets [65]. However, these approaches limit the scalability of the CS process in polymer electronics, requiring specialized equipment and environments, which complicates the integration of CS into existing manufacturing lines. Consequently, there is a pressing need for innovative solutions to streamline the CS process, reduce dependency on specialized environments, and lower the barriers to fully exploit CS technology in the fields of TENG and polymer electronics. Accordingly, the next section is dedicated to a case study on a manufacturing innovation aimed at increasing the line resolution of the CS process without the need for dedicated masking and vacuum equipment.

3.5. *Case study: CS-based manufacturing innovation for polymer electronics*

A manufacturing pathway, as shown in Fig. 8, is proposed to improve the resolution of traditional CS, enabling the creation of free-form electronic circuitry on 3D-printed polymers. The manufacturing process can be summarized as follows: First, a customized circuitry, such as an LED display counter circuit, is designed (see Fig. S13, Supporting Information) and incorporated into the material extrusion 3-D printing process. This process involves the incorporation of groove patterns for precise circuitry design (Fig. 8**,** left panel). The grooves feature a 1 mm linewidth and 1.5 mm depth. Next, the surface of the 3D-printed part is metallized through CS particle deposition (Fig. 8**,** middle panel). The high-speed impingement of particles during the robotic-controlled CS process allows the particles to penetrate the grooves, forming electrically conductive metallization within these structures (see Video S4). Finally, the as-CS surface is polished to remove the Sn layer (≈ 0.5 mm-thick) from the surface while retaining the electrodes inside the grooves (Fig. 9**,** right panel). This approach enables the creation of free-form high-resolution electrodes embedded into the 3D-printed part surface, ensuring consistent electrical conductivity (see Fig. 9**a**), which is essential for the development of 3-D plastronic devices.

The resulting custom-build electrodes can be utilized in surface-mount devices (SMD), enabling modular assembly of the circuits. In this context, an adjustable LED circuit was designed on the 3D-printed part (Fig. S13, Supporting Information). Various circuit components (e.g., resistor, capacitor, button, display) were assembled on the 3D-printed board by applying silver epoxy (*MG Chemicals*) to the junction points (Fig. 9**a**). A DC power unit (*Korad, KD6003D*) was used to power the circuit with an input voltage of 12 V. Fig. 9**b** and Video S5 (Supporting Information) illustrate the implementation of an adjustable LED display counter circuit on the 3D-printed part in Fig. 8 (right panel), verifying the electrical functionality of the circuitry. As such, the case study demonstrates that the application scope of the CS can expand from large-area functional surface coatings to free-form, custom-designed electronics on 3D-printed polymers with line resolution of up to 1 mm. Notably, the resolution of the electrodes could be further enhanced by adopting high-resolution printing techniques such as vat polymerization. Furthermore, owing to the multi-axis robot arm compatibility of the CS process, functional surface structures on freeform 3-D printed parts (e.g., dome-shaped, convex-concave) can be effectively created without the need for dedicated vacuum equipment [65]. This capability further underscores the potential of this emerging manufacturing technique for processing intricate surface structures.

Besides, this approach could extend beyond 3D-printed polymer parts to various commercial thermoplastic polymers, including ABS, PETG, PEEK, and more. Fig. S14 demonstrates the electrodes fabricated on 3D-printed ABS and PETG, illustrating consistent and promising electrical conductivity. Unlike the conventional polymer metallization techniques, CS writing could eliminate the need for chemical etching,

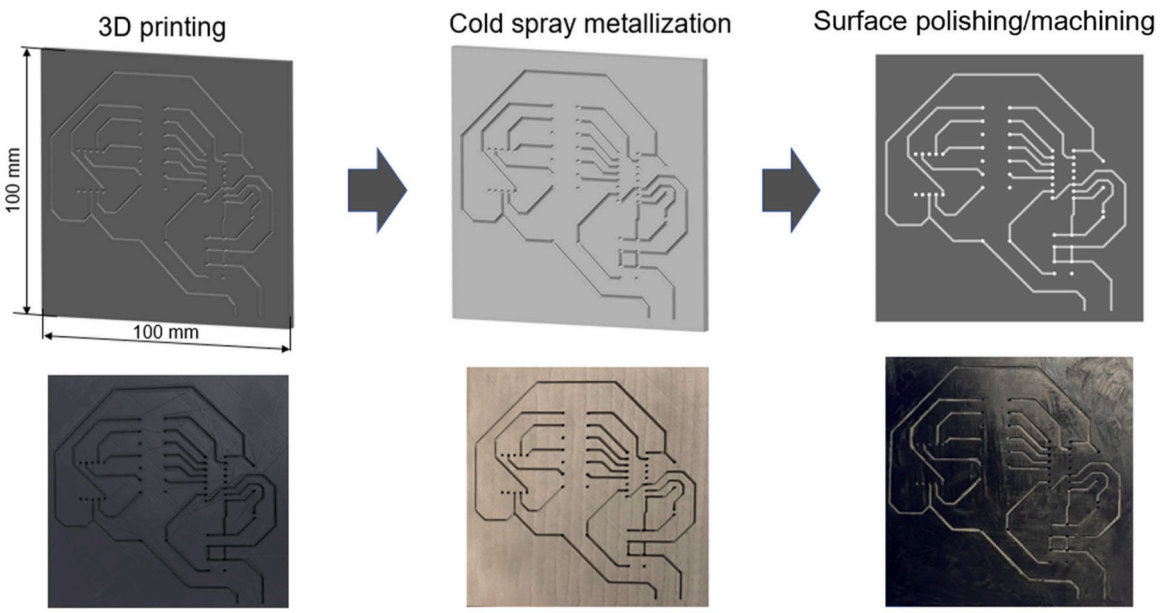

Fig. 8. A manufacturing pathway for CS-based polymer electronics; schematics (top panel) and representative images (bottom panel).

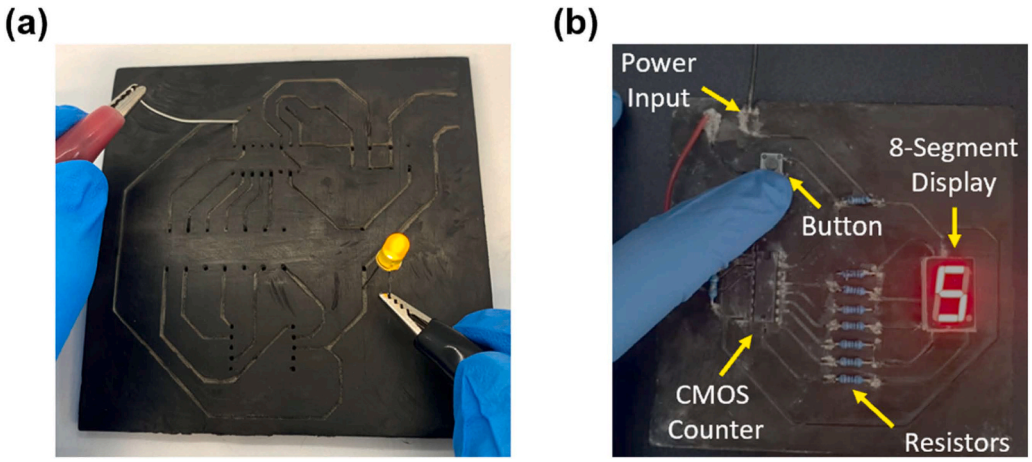

Fig. 9. (a) Fabricated custom-designed electrodes embedded into the 3D-printed part; (b) Representative image of the LED display counter on the 3D-printed part.

palladium (Pd) seeding, and post-curing processes, making it an eco-friendly choice for 3D-printed electronics. Given the high interest in integrating electronics, sensors, and energy harvesting devices for IoT and Industry 4.0, this approach offers a robust solution for creating 3D-printed parts with integrated electronic circuits.

4. Conclusion

We employed a complete AM approach for creating functionalized electrodes on 3D-printed parts, specifically tailored for triboelectric energy harvesting applications. In this approach, we integrated material extrusion 3D printing and the CS technique to develop high-performance functional electrodes. First, the polymer PLA substrates were 3D printed. Next, the conductive electrodes were directly written on the polymer surface by the CS. Process-structure-property relationships of the CS were uncovered for one-step fabrication of functionalized electrodes on 3D-printed polymer parts for TENG applications. Furthermore, a manufacturing pathway was proposed to address the low-spatial resolution of the CS metallization, aiming to achieve polymer electronics with high-line resolution. The following conclusions can be drawn:

- Unlike the traditional polymer metallization techniques, the AM approach in this work eliminates the need for chemical-etching, masking, precursor, or vacuum processes, thereby offering potential for sustainable manufacturing of functionalized electrodes on 3D-printed parts.
- The resulting electrodes exhibited promising characteristics, including electrical conductivity (9.8×10^4 S.m^{-1}), surface roughness ($R_a = 6.32$ μm), adhesive strength, charge storage capacity (9.0 ± 1.4 mC.cm^{-2}), and stability.
- The TENGs with the fabricated electrodes led to significantly higher energy harvesting performance (≈ 1.85–2.9-fold) than that of the control TENGs.
- The TENG with the CS electrode (PLA/Sn) can achieve the maximum open-circuit output voltage of 174, the short-circuit density of ≈ 55 mA/m^2, and the power density of 1676 mW/m^2.
- A manufacturing strategy combining material extrusion 3D printing with CS and subsequent surface machining enhanced electrode line resolution to 1 mm.
- The results reveal that the established AM platform holds significant promise for advancing the field of TENG and polymer electronics by

addressing the limitations of traditional electrode manufacturing techniques.

Supporting information

Figs. S1–S14 show the feasibility test of CS Al deposition on 3D-printed PLA; IR camera images of the nozzle at various gas temperature settings; photographs and SEM images of the as-CS specimens; cross-section SEM images of the as-CS specimens; EDX results of the fabricated electrodes; image of the CV test setup; the image of the pneumatic actuator used in the TENG characterization; the voltage output results of the TENGs for additional characterizations; the schematic of the full-bridge rectifier used in the TENG tests; the images of the TENG-driven LED circuit; and circuit diagram of the LED display counter; the images of the as-CS Sn electrode on 3D-printed ABS and PETG parts.

Author contributions

The manuscript was written through contributions of all authors. All authors have given approval to the final version of the manuscript.

CRediT authorship contribution statement

Martin Byung-Guk Jun: Writing – review & editing, Validation, Supervision, Resources, Conceptualization. **Chi Hwan Lee:** Writing – review & editing, Validation, Supervision, Resources, Conceptualization. **Johnson Samuel:** Writing – review & editing, Validation, Resources. **Wenzhuo Wu:** Writing – review & editing, Validation, Supervision, Resources. **Hyowon Lee:** Writing – review & editing, Supervision, Resources. **Chandra Nath:** Writing – review & editing, Supervision. **Jung-Ting Tsai:** Methodology, Investigation. **Jiho Lee:** Investigation, Formal analysis. **Yuseop Sim:** Methodology, Investigation. **Jongcheon Lim:** Validation, Investigation, Formal analysis. **Shujia Xu:** Writing – review & editing, Validation, Investigation. **Young Won Kim:** Writing – review & editing, Validation, Investigation, Formal analysis, Data curation. **Sk Shamim Hasan Abir:** Writing – original draft, Visualization, Validation, Methodology, Investigation, Formal analysis. **Taehoo Chang:** Writing – original draft, Visualization, Methodology, Investigation, Formal analysis, Data curation. **Semih Akin:** Writing – review & editing, Writing – original draft, Visualization, Validation, Supervision, Software, Resources, Project administration, Methodology, Investigation, Formal analysis, Data curation, Conceptualization.

Declaration of Competing Interest

The authors declare the following financial interests/personal relationships which may be considered as potential competing interests: Martin Jun & Semih Akin has patent Cold spray printed flexible electronics and method for manufacturing the same pending to Purdue Research Foundation (West Lafayette, IN, US). If there are other authors, they declare that they have no known competing financial interests or personal relationships that could have appeared to influence the work reported in this paper.

Data Availability

Data will be made available on request.

Appendix A. Supporting information

Supplementary data associated with this article can be found in the online version at doi:10.1016/j.nanoen.2024.110082.

References

[1] Z.L. Wang, T. Jiang, L. Xu, Toward the blue energy dream by triboelectric nanogenerator networks, Nano Energy 39 (2017) 9–23, https://doi.org/10.1016/j.nanoen.2017.06.035.

[2] C. Wu, A.C. Wang, W. Ding, H. Guo, Z.L. Wang, Triboelectric nanogenerator: a foundation of the energy for the new era, Adv. Energy Mater. 9 (2019) 1802906, https://doi.org/10.1002/aenm.201802906.

[3] Z.L. Wang, Triboelectric nanogenerator (TENG)—sparking an energy and sensor revolution, Adv. Energy Mater. 10 (2020) 2000137, https://doi.org/10.1002/aenm.202000137.

[4] S. Wang, L. Lin, Z.L. Wang, Triboelectric nanogenerators as self-powered active sensors, Nano Energy 11 (2015) 436–462, https://doi.org/10.1016/j.nanoen.2014.10.034.

[5] J. Deng, Z. Wu, X. Huo, Y. Chen, H. Qian, T. Tang, X. Ge, Y. Wang, Triboelectric based smart ceramic tiles, Nano Energy 128 (2024), https://doi.org/10.1016/j.nanoen.2024.109928.

[6] Y.W. Kim, S. Akin, H. Yun, S. Xu, W. Wu, M. Byung, G. Jun, Enhanced performance of triboelectric nanogenerators and sensors via cold spray particle deposition, ACS Appl. Mater. Interfaces (2022), https://doi.org/10.1021/ACSAMI.2C09367.

[7] S. Cai, C. Han, Z. Cao, Y. Chen, J. Cao, Y. Wang, Z. Wu, Three-dimensional triboelectric nanogenerator manufacturing using water transfer printing, Chem. Eng. J. 493 (2024), https://doi.org/10.1016/j.cej.2024.152862.

[8] H. Zhang, Structures of triboelectric nanogenerators, in: Flexible and Stretchable Triboelectric Nanogenerator Devices: Toward Self-Powered Systems, John Wiley & Sons, Ltd, 2019, pp. 19–40, https://doi.org/10.1002/9783527820153.ch2.

[9] M. Kim, S. Lee, V.A. Cao, M.C. Kim, J. Nah, Performance enhancement of triboelectric nanogenerators via photo-generated carriers using a polymer-perovskite composite, Nano Energy 112 (2023) 108474, https://doi.org/10.1016/J.NANOEN.2023.108474.

[10] X.W. Zhang, G.Z. Li, G.G. Wang, J.L. Tian, Y.L. Liu, D.M. Ye, Z. Liu, H.Y. Zhang, J. C. Han, High-performance triboelectric nanogenerator with double-surface shape-complementary microstructures prepared by using simple sandpaper templates, ACS Sustain Chem. Eng. 6 (2018) 2283–2291, https://doi.org/10.1021/acssuschemeng.7b03745.

[11] R. Zhang, H. Olin, Material choices for triboelectric nanogenerators: a critical review, EcoMat 2 (2020) e12062, https://doi.org/10.1002/EOM2.12062.

[12] Z. Zhao, L. Zhou, S. Li, D. Liu, Y. Li, Y. Gao, Y. Liu, Y. Dai, J. Wang, Z.L. Wang, Selection rules of triboelectric materials for direct-current triboelectric nanogenerator, Nat. Commun. 12 (2021) 1–8, https://doi.org/10.1038/s41467-021-25046-z.

[13] D.W. Kim, J.H. Lee, J.K. Kim, U. Jeong, Material aspects of triboelectric energy generation and sensors, NPG Asia Mater. 12 (2020) 1–17, https://doi.org/10.1038/s41427-019-0176-0.

[14] A. Chen, C. Zhang, G. Zhu, Z.L. Wang, Polymer materials for high-performance triboelectric nanogenerators, Adv. Sci. 7 (2020), https://doi.org/10.1002/advs.202000186.

[15] H.J. Yang, J.W. Lee, S.H. Seo, B. Jeong, B. Lee, W.J. Do, J.H. Kim, J.Y. Cho, A. Jo, H.J. Jeong, S.Y. Jeong, G.H. Kim, G.W. Lee, Y.E. Shin, H. Ko, J.T. Han, J.H. Park, Fully stretchable self-charging power unit with micro-supercapacitor and triboelectric nanogenerator based on oxidized single-walled carbon nanotube/polymer electrodes, Nano Energy 86 (2021) 106083, https://doi.org/10.1016/J.NANOEN.2021.106083.

[16] G. Li, J. Zhang, F. Huang, S. Wu, C.H. Wang, S. Peng, Transparent, stretchable and high-performance triboelectric nanogenerator based on dehydration-free ionically conductive solid polymer electrode, Nano Energy 88 (2021) 106289, https://doi.org/10.1016/J.NANOEN.2021.106289.

[17] C. Credi, R. Bernasconi, M. Levi, L. Magagnin, Self-activating metal-polymer composites for the straightforward selective metallization of 3D printed parts by stereolithography, J. Mater. Res. Technol. 22 (2023) 1855–1867, https://doi.org/10.1016/j.jmrt.2022.12.035.

[18] T. Duguet, F. Senocq, L. Laffont, C. Vahlas, Metallization of polymer composites by metalorganic chemical vapor deposition of Cu: surface functionalization driven films characteristics, Surf. Coat. Technol. 230 (2013) 254–259, https://doi.org/10.1016/j.surfcoat.2013.06.065.

[19] P. He, J. Cao, H. Ding, C. Liu, J. Neilson, Z. Li, I.A. Kinloch, B. Derby, Screen-printing of a highly conductive graphene ink for flexible printed electronics, ACS Appl. Mater. Interfaces 11 (2019) 32225–32234, https://doi.org/10.1021/acsami.9b04589.

[20] L. Nayak, S. Mohanty, S.K. Nayak, A. Ramadoss, A review on inkjet printing of nanoparticle inks for flexible electronics, J. Mater. Chem. C Mater. 7 (2019) 8771–8795, https://doi.org/10.1039/c9tc01630a.

[21] S. Akin, T. Gabor, S. Jo, H. Joe, J.T. Tsai, Y. Park, C.H. Lee, M.S. Park, M.B.G. Jun, Dual regime spray deposition based laser direct writing of metal patterns on polymer substrates, J. Micro Nanomanuf. 8 (2020), https://doi.org/10.1115/1.4046282.

[22] R. Melentiev, A. Yudhanto, R. Tao, T. Vuchkov, G. Lubineau, Metallization of polymers and composites: state-of-the-art approaches, Mater. Des. 221 (2022) 110958, https://doi.org/10.1016/J.MATDES.2022.110958.

[23] A. Ahmed, A. Azam, Y. Wang, Z. Zhang, N. Li, C. Jia, R.T. Mushtaq, M. Rehman, T. Gueye, M.B. Shahid, B.A. Wajid, Additively manufactured nano-mechanical energy harvesting systems: advancements, potential applications, challenges and future perspectives, Nano Converg. 8 (2021), https://doi.org/10.1186/s40580-021-00289-0.

[24] A.T.K. Perera, K. Wu, W.Y. Wan, K. Song, X. Meng, S. Umezu, Y. Wang, H. Sato, Modified polymer 3D printing enables the formation of functionalized micro-

metallic architectures, Addit. Manuf. 61 (2023) 103317, https://doi.org/10.1016/j.addma.2022.103317.
[25] K. Song, Y. Cui, T. Tao, X. Meng, M. Sone, M. Yoshino, S. Umezu, H. Sato, New metal-plastic hybrid additive manufacturing for precise fabrication of arbitrary metal patterns on external and even internal surfaces of 3D plastic structures, ACS Appl. Mater. Interfaces 14 (2022) 46896–46911, https://doi.org/10.1021/acsami.2c10617.
[26] D.J. Roach, C. Roberts, J. Wong, X. Kuang, J. Kovitz, Q. Zhang, T.G. Spence, H. J. Qi, Surface modification of fused filament fabrication (FFF) 3D printed substrates by inkjet printing polyimide for printed electronics, Addit. Manuf. 36 (2020) 101544, https://doi.org/10.1016/j.addma.2020.101544.
[27] K. Angel, H.H. Tsang, S.S. Bedair, G.L. Smith, N. Lazarus, Selective electroplating of 3D printed parts, Addit. Manuf. 20 (2018) 164–172, https://doi.org/10.1016/j.addma.2018.01.006.
[28] P.F. Flowers, C. Reyes, S. Ye, M.J. Kim, B.J. Wiley, 3D printing electronic components and circuits with conductive thermoplastic filament, Addit. Manuf. 18 (2017) 156–163, https://doi.org/10.1016/j.addma.2017.10.002.
[29] M.J. Kim, M.A. Cruz, S. Ye, A.L. Gray, G.L. Smith, N. Lazarus, C.J. Walker, H. H. Sigmarsson, B.J. Wiley, One-step electrodeposition of copper on conductive 3D printed objects, Addit. Manuf. 27 (2019) 318–326, https://doi.org/10.1016/j.addma.2019.03.016.
[30] J. Zhan, T. Tamura, X. Li, Z. Ma, M. Sone, M. Yoshino, S. Umezu, H. Sato, Metal-plastic hybrid 3D printing using catalyst-loaded filament and electroless plating, Addit. Manuf. 36 (2020) 101556, https://doi.org/10.1016/j.addma.2020.101556.
[31] X. Tang, C. Bi, C. Han, B. Zhang, A new palladium-free surface activation process for Ni electroless plating on ABS plastic, Mater. Lett. 63 (2009) 840–842, https://doi.org/10.1016/j.matlet.2009.01.006.
[32] N. Lazarus, J.B. Tyler, J.A. Cardenas, B. Hanrahan, H. Tsang, S.S. Bedair, Direct electroless plating of conductive thermoplastics for selective metallization of 3D printed parts, Addit. Manuf. 55 (2022) 102793, https://doi.org/10.1016/j.addma.2022.102793.
[33] S. Akin, Y.W. Kim, S. Xu, C. Nath, W. Wu, M.B.G. Jun, Cold spray direct writing of flexible electrodes for enhanced performance triboelectric nanogenerators, J. Manuf. Process (2023), https://doi.org/10.1016/j.jmapro.2023.05.015.
[34] S. Akin, S. Kim, C.K. Song, S.Y. Nam, M.B.-G. Jun, Fully additively manufactured counter electrodes for dye-sensitized solar cells, Micromachines 15 (2024) 464, https://doi.org/10.3390/mi15040464.
[35] R. Della Gatta, A.S. Perna, A. Viscusi, G. Pasquino, A. Astarita, Cold spray deposition of metallic coatings on polymers: a review, J. Mater. Sci. 57 (2022) 27–57, https://doi.org/10.1007/s10853-021-06561-2.
[36] S. Akin, S. Jo, M.B.G. Jun, A cold spray-based novel manufacturing route for flexible electronics, J. Manuf. Process 86 (2023) 98–108, https://doi.org/10.1016/j.jmapro.2022.12.035.
[37] J.T. Tsai, S. Akin, D.F. Bahr, M.B.G. Jun, A predictive modeling approach for cold spray metallization on polymers, Surf. Coat. Technol. 483 (2024), https://doi.org/10.1016/j.surfcoat.2024.130711.
[38] S. Milovanovic, J. Pajnik, I. Lukic, Tailoring of advanced poly(lactic acid)-based materials: a review, J. Appl. Polym. Sci. 139 (2022) 51839, https://doi.org/10.1002/app.51839.
[39] S. Liu, W. Zheng, B. Yang, X. Tao, Triboelectric charge density of porous and deformable fabrics made from polymer fibers, Nano Energy 53 (2018) 383–390, https://doi.org/10.1016/j.nanoen.2018.08.071.
[40] S. Chao, H. Ouyang, D. Jiang, Y. Fan, Z. Li, Triboelectric nanogenerator based on degradable materials, EcoMat 3 (2021), https://doi.org/10.1002/eom2.12072.
[41] L.N.Y. Cao, E. Su, Z. Xu, Z.L. Wang, Fully enclosed microbeads structured TENG arrays for omnidirectional wind energy harvesting with a portable galloping oscillator, Mater. Today 71 (2023) 9–21, https://doi.org/10.1016/j.mattod.2023.11.001.
[42] R. Nikbakht, M. Saadati, T.S. Kim, M. Jahazi, H.S. Kim, B. Jodoin, Cold spray deposition characteristic and bonding of CrMnCoFeNi high entropy alloy, Surf. Coat. Technol. 425 (2021) 127748, https://doi.org/10.1016/J.SURFCOAT.2021.127748.
[43] S. Akin, S. Lee, S. Jo, D.G. Ruzgar, K. Subramaniam, J.-T. Tsai, M.B.-G. Jun, Cold spray-based rapid and scalable production of printed flexible electronics, Addit. Manuf. 60 (2022) 103244, https://doi.org/10.1016/J.ADDMA.2022.103244.
[44] H. Zou, L. Guo, H. Xue, Y. Zhang, X. Shen, X. Liu, P. Wang, X. He, G. Dai, P. Jiang, H. Zheng, B. Zhang, C. Xu, Z.L. Wang, Quantifying and understanding the triboelectric series of inorganic non-metallic materials, Nat. Commun. 11 (2020) 1–7, https://doi.org/10.1038/s41467-020-15926-1.
[45] A. Cano-Vicent, M.M. Tambuwala, S.S. Hassan, D. Barh, A.A.A. Aljabali, M. Birkett, A. Arjunan, Á. Serrano-Aroca, Fused deposition modelling: current status, methodology, applications and future prospects, Addit. Manuf. 47 (2021) 102378, https://doi.org/10.1016/j.addma.2021.102378.
[46] R. Melentiev, N. Yu, G. Lubineau, Polymer metallization via cold spray additive manufacturing: a review of process control, coating qualities, and prospective applications, Addit. Manuf. 48 (2021) 102459, https://doi.org/10.1016/j.addma.2021.102459.
[47] W.Y. Li, C. Zhang, X.P. Guo, G. Zhang, H.L. Liao, C.J. Li, C. Coddet, Effect of standoff distance on coating deposition characteristics in cold spraying, Mater. Des. 29 (2008) 297–304, https://doi.org/10.1016/j.matdes.2007.02.005.
[48] S. Akin, P. Wu, J.-T. Tsai, C. Nath, J. Chen, M.B.-G. Jun, A study on droplets dispersion and deposition characteristics under supersonic spray flow for nanomaterial coating applications, Surf. Coat. Technol. 426 (2021) 127788, https://doi.org/10.1016/j.surfcoat.2021.127788.
[49] S. Yin, X.F. Wang, W.Y. Li, B.P. Xu, Numerical study on the effect of substrate angle on particle impact velocity and normal velocity component in cold gas dynamic spraying based on CFD, J. Therm. Spray. Technol. 19 (2010) 1155–1162, https://doi.org/10.1007/s11666-010-9510-3.
[50] S. Seok, H.D. Park, J. Kim, Characterization and analysis of metal adhesion to Parylene polymer substrate using scotch tape test for peripheral neural probe, Micromachines 11 (2020) 605, https://doi.org/10.3390/MI11060605.
[51] S.N.F. Zainudin, H. Abdullah, M. Markom, Electrochemical studies of tin oxide based-dye-sensitized solar cells (DSSC): a review, J. Mater. Sci. Mater. Electron. 30 (2019) 5342–5356, https://doi.org/10.1007/s10854-019-00929-6.
[52] K. Saranya, M. Rameez, A. Subramania, Developments in conducting polymer based counter electrodes for dye-sensitized solar cells - an overview, Eur. Polym. J. 66 (2015) 207–227, https://doi.org/10.1016/j.eurpolymj.2015.01.049.
[53] S.F. Cogan, Neural stimulation and recording electrodes, Annu Rev. Biomed. Eng. 10 (2008) 275–309, https://doi.org/10.1146/annurev.bioeng.10.061807.160518.
[54] Z.L. Wang, L. Lin, J. Chen, S. Niu, Y. Zi, Triboelectric Nanogenerator: Vertical Contact-Separation Mode, in: 2016: pp. 23–47. https://doi.org/10.1007/978-3-319-40039-6_2.
[55] S. Niu, S. Wang, L. Lin, Y. Liu, Y.S. Zhou, Y. Hu, Z.L. Wang, Theoretical study of contact-mode triboelectric nanogenerators as an effective power source, Energy Environ. Sci. 6 (2013) 3576–3583, https://doi.org/10.1039/c3ee42571a.
[56] H. Zou, Y. Zhang, L. Guo, P. Wang, X. He, G. Dai, H. Zheng, C. Chen, A.C. Wang, C. Xu, Z.L. Wang, Quantifying the triboelectric series, Nat. Commun. 10 (2019) 1–9, https://doi.org/10.1038/s41467-019-09461-x.
[57] Z.L. Wang, A.C. Wang, On the origin of contact-electrification, Mater. Today 30 (2019) 34–51, https://doi.org/10.1016/j.mattod.2019.05.016.
[58] B. Dudem, D.H. Kim, A.R. Mule, J.S. Yu, Enhanced performance of microarchitectured PTFE-based triboelectric nanogenerator via simple thermal imprinting lithography for self-powered electronics, ACS Appl. Mater. Interfaces 10 (2018) 24181–24192, https://doi.org/10.1021/acsami.8b06295.
[59] B. Fan, G. Liu, X. Fu, Z. Wang, Z. Zhang, C. Zhang, Composite film with hollow hierarchical silica/perfluoropolyether filler and surface etching for performance enhanced triboelectric nanogenerators, Chem. Eng. J. 446 (2022) 137263, https://doi.org/10.1016/J.CEJ.2022.137263.
[60] M. Mariello, E. Scarpa, L. Algieri, F. Guido, V.M. Mastronardi, A. Qualtieri, M. De Vittorio, Novel flexible triboelectric nanogenerator based on metallized porous PDMS and Parylene C, Energy 13 (2020) 1625, https://doi.org/10.3390/EN13071625.
[61] X. Shen, W. Han, Y. Jiang, Q. Ding, X. Li, X. Zhao, Z. Li, Punching pores on cellulose fiber paper as the spacer of triboelectric nanogenerator for monitoring human motion, Energy Rep. 6 (2020) 2851–2860, https://doi.org/10.1016/j.egyr.2020.10.011.
[62] T. Gabor, S. Akin, M.B.G. Jun, Numerical studies on cold spray gas dynamics and powder flow in circular and rectangular nozzles, J. Manuf. Process 114 (2024) 232–246, https://doi.org/10.1016/j.jmapro.2024.02.005.
[63] W. Chen, Y. Yu, J. Ma, S. Zhu, W. Liu, J. Yang, Low-pressure cold spraying of copper–graphite solid lubricating coatings on aluminum alloy 7075-T651, J. Therm. Spray. Technol. 28 (2019) 1688–1698, https://doi.org/10.1007/s11666-019-00905-w.
[64] S.G. Bierschenk, D. Kovar, A nozzle design for mitigating particle slowing in the bow shock region during micro-cold spray of 8 YSZ films, J. Aerosol Sci. 179 (2024), https://doi.org/10.1016/j.jaerosci.2024.106360.
[65] S. Akin, C. Nath, M.B.-G. Jun, Selective surface metallization of 3D-printed polymers by cold-spray-assisted electroless deposition, ACS Appl. Electron Mater. (2023), https://doi.org/10.1021/acsaelm.3c00893.
[66] Fluorine Doped Tin Oxide Coated Glass Slide L × W × D 300 mm × 300 mm × 2.2 mm, Surface Resistivity 7 o/sq FTO glass, (n.d.). ⟨https://www.sigmaaldrich.com/US/en/product/aldrich/735167⟩ (accessed January 26, 2023).
[67] Sigma Aldrich, Indium tin oxide coated PET surface resistivity 60 Ω/sq, L × W × thickness 1 ft × 1 ft × 5 mil, sheet | Sigma-Aldrich, (n.d.). ⟨https://www.sigmaaldrich.com/US/en/product/aldrich/639303⟩ (accessed April 15, 2022).
[68] F.S. Oliveira, R.B. Cipriano, F.T. da Silva, E.C. Romão, C.A.M. dos Santos, Simple analytical method for determining electrical resistivity and sheet resistance using the van der Pauw procedure, Sci. Rep. 10 (2020) 1–8, https://doi.org/10.1038/s41598-020-72097-1.

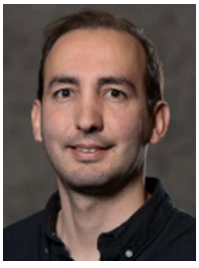

Dr. Semih Akin is an Assistant Professor of Mechanical Engineering at Rensselaer Polytechnic Institute (RPI) (New York, USA). He received his Ph.D. from Purdue University, West Lafayette, USA in 2022, where he also worked as a Postdoctoral Fellow before joining RPI. His current research interests center around surface engineering and advanced multi-scale manufacturing, with applications in 3D-printed electronics, smart structures, electronic textiles, and energy devices. His contributions have been recognized with awards, including the 2023 Outstanding Graduate Student Research Award, the 2022 Ward. A. Lambert Fellowship from Purdue University CoE, and the 2021 Best Paper Award in the World Congress on Micro and Nano Manufacturing.

Dr. Taehoo Chang is currently a yield development engineer at Intel Corporation. He received the BSc in Metallurgical Engineering and M.S. degrees in Materials Science and Engineering from Yonsei University, Seoul, South Korea in 2012 and 2014, respectively. He then received his PhD degree in 2023 from Purdue University in the School of Materials Engineering. His main research focus is on flexible electronic devices, smart manufacturing processes and automation of FIB/TEM technologies.

Sk Shamim Hasan Abir is currently a graduate research assistant in mechanical engineering department at Rensselaer Polytechnic Institute (RPI). He received his mechanical engineering master's (2021) from the University of Texas Rio Grande Valley, and bachelor's degree (2017) from Bangladesh University of Engineering and Technology. His research interests include ceramic sintering, polymer nanocomposite, piezo/triboelectric nanogenerator, flexible electronics, and biosensors. He was awarded the Presidential Graduate Research Assistantship (2019–2021), Margaret Draper Scholarships (2020), and AT&T-UTPA Scholarships (2021).

Dr. Young Won Kim is currently a Senior Researcher at the Korea Additive Manufacturing Technology Innovation Center (KAMIC, KITECH). He received his B.S. and Ph.D. degrees from Hanyang University, South Korea, in 2015 and 2019, respectively. Prior to his current position, he worked as a postdoctoral researcher at both Purdue University and KITECH. His current research focuses on the digitalization, intelligence, and standardization of 3D printing data. His research interests include machine learning, energy harvesting, piezo and triboelectric devices, and 3D metal printing.

Shujia Xu received his BS degree in Mechanical Engineering in 2015 form South China University of Technology (SCUT), MS degree in Biomedical Engineering in 2018 from Sun Yat-Sen University (SYSU), and PhD degree in Industrial Engineering in 2024 from Purdue University. His research interests include materials and manufacturing innovations of wearable electronics for human-integrated applications, including healthcare, human-machine interface, VR, and AI.

Dr. Jongcheon Lim is currently a postdoctoral research fellow at The University of Texas Health Science Center at Houston and Rice University Neuroengineering Initiative. He received his Ph.D. in Biomedical Engineering from Purdue University, West Lafayette, USA in 2023. His research experience includes microfabrication of neural interface devices, novel microelectrodes for neural stimulation and recording, mechanics of soft materials, and hydrogel-based bioelectronic interface. He is currently working towards developing next-generation clinical neuroelectronic devices.

Yuseop Sim is a Ph.D. student in the Department of Mechanical Engineering at Purdue University, West Lafayette, IN, USA. He received M.S. degree in the Department of Mechanical Engineering from Kyungpook National University, Daegu, Korea, in 2022. His research interests include system monitoring, smart manufacturing systems, acoustics, and robotics.

Dr. Jiho Lee is a postdoctoral research assistant in the Department of Mechanical Engineering at Purdue University, West Lafayette, IN, USA. He received Ph.D. in the Department of Mechanical Engineering from Sungkyunkwan University, Suwon, Korea, in 2023. His research interests include smart and secure manufacturing systems with advanced artificial intelligence, cold spray additive manufacturing, and hybrid manufacturing processes.

Dr. Jung-Ting Tsai is an assistant professor in the Mechanical Department at the National Taiwan University of Science and Technology (NTUST). He was a post-doctoral fellow in the Applied Materials Division at Argonne National Laboratory from 2022 to 2023. He received his Ph.D. in Materials Engineering from Purdue University in 2021. His lead author on the cold spray manuscript has been selected as an Editor's Choice article by the Journal of Thermal Spray Technology in 2021. In addition, he is the recipient of the International Thermal Spray Association Graduate Scholarship.

Dr. Chandra Nath, a Senior Researcher in Environmental and Ecological Engineering at Purdue, has 20 years of experience in academia and industry with smart, sustainable, energy-efficient, and eco-friendly design and manufacturing methods, and their adoption and commercialization. He published over 70 journals and conferences, three book chapters, and several patents. He received awards, e.g., SME Outstanding Young Manufacturing Engineer (2014), ASME Best Paper (2013), Young Researcher in ASPEN (2009), '25 leaders transforming manufacturing' (SME magazine, 2022), and the like. He received a Ph.D. degree from NUS, Singapore (2009), and a B.Sc. degree from Bangladesh University of Engineering and Technology, Bangladesh (2004), both in mechanical engineering.

Dr. Hyowon "Hugh" Lee received the M.S. and Ph.D. degrees in biomedical engineering from the University of California, Los Angeles, CA, USA, in 2008 and 2011, respectively. Before joining Purdue, he was a Senior Process Engineer for St. Jude Medical's Implantable Electronic Systems Division where he worked on implantable electronic devices. His current research interests center around improving the reliability and functionality of implantable sensors and actuators for various medical conditions including neurodegeneration, stroke, and opioid use disorder. He was the recipient of the NSF CAREER Award, and his lab is supported by NIH, NINDS, NIDA, NSF, Indiana CTSI, Samsung, and Eli Lilly.

Dr. Wenzhuo Wu is the Ravi and Eleanor Talwar Rising Star Associate Professor in the School of Industrial Engineering at Purdue University. Dr. Wu received his Ph.D. from Georgia Tech in Materials Science and Engineering. Dr. Wu's research focuses on manufacturable nanotechnologies for energy, electronics, and wearable devices. He was a recipient of many awards, such as SME Outstanding Young Manufacturing Engineer Award, Advanced Materials Interfaces Hall of Fame, ARO Young Investigator Award, NSF Early CAREER Award, Advanced Materials Technologies Hall of Fame, and Sensors Young Investigator Award.

Dr. Johnson Samuel is a Professor of Mechanical Engineering at Rensselaer Polytechnic Institute (New York, USA). As director of the Nano/Micro-scale Manufacturing and Material Design Lab (NanoM3 Design Lab) at Rensselaer, he leads research and education efforts in the areas of advanced manufacturing and material design. His current interests include additive manufacturing of metal and polymer systems; multi-material co-builds, and applied robotics. He is the recipient of the Richard Skalak Award - ASME Bioengineering Division (2024), and NSF CAREER award (2014). He currently serves on the ASME Manufacturing Engineering Division's executive committee (2023–2028) and is also an active member of the Society of Manufacturing Engineers.

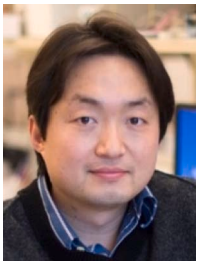

Dr. Chi Hwan Lee is the Leslie A. Geddes Professor at Purdue University, holding positions in both Biomedical Engineering and Mechanical Engineering. After earning a Ph.D. in Mechanical Engineering from Stanford University in 2013, Dr. Lee continued his research journey at the University of Illinois at Urbana-Champaign as a postdoctoral assistant before joining Purdue University in 2015. Drawing upon his expertise, he has spearheaded innovative wearable devices that address clinical needs with simplicity and effectiveness. He has been recognized for his efforts with awards, including the 2021 Sensors Young Investigator Award, 2020 Purdue CoE Early Career Research Award, and 2019 NIH Trailblazer Award. Dr. Lee has published over 90 journal papers and 6 book chapters, secured 6 U.S. patents, filed 11 utility patents, and co-founded multiple startup companies.

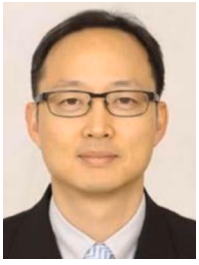

Dr. Martin Jun is a Professor of the School of Mechanical Engineering at Purdue University, West Lafayette, IN, USA. He received his PhD degree in 2005 from the University of Illinois at Urbana-Champaign in the Department of Mechanical Science and Engineering. His main research focus is on advanced multi-scale and smart manufacturing processes and technologies for various applications. He has authored over 160 peer-reviewed journal publications. He is also the recipient of the 2011 SME Outstanding Young Manufacturing Engineer Award, 2012 Canadian Society of Mechanical Engineers I.W. Smith Award for Outstanding Achievements, and 2015 Korean Society of Manufacturing Technology Engineers Damwoo Award. He has also been recognized as 20 most influential academics and 25 leaders transforming manufacturing in the Smart Manufacturing magazine.